



# Electrochemical impedance spectroscopy study of the passive film for laser-beam-melted 17-4PH stainless steel

Adrien Barroux, Julien Delgado, Mark E. Orazem, Bernard Tribollet, Lydia Laffont, Christine Blanc

## ► To cite this version:

Adrien Barroux, Julien Delgado, Mark E. Orazem, Bernard Tribollet, Lydia Laffont, et al.. Electrochemical impedance spectroscopy study of the passive film for laser-beam-melted 17-4PH stainless steel. Corrosion Science, 2021, 191, pp.109750. 10.1016/j.corsci.2021.109750 . hal-03352528

**HAL Id: hal-03352528**

**<https://hal.science/hal-03352528>**

Submitted on 23 Sep 2021

**HAL** is a multi-disciplinary open access archive for the deposit and dissemination of scientific research documents, whether they are published or not. The documents may come from teaching and research institutions in France or abroad, or from public or private research centers.

L'archive ouverte pluridisciplinaire **HAL**, est destinée au dépôt et à la diffusion de documents scientifiques de niveau recherche, publiés ou non, émanant des établissements d'enseignement et de recherche français ou étrangers, des laboratoires publics ou privés.






## Open Archive Toulouse Archive Ouverte (OATAO)

OATAO is an open access repository that collects the work of Toulouse researchers and makes it freely available over the web where possible

This is an author's version published in: <http://oatao.univ-toulouse.fr/28306>

**Official URL:** <https://doi.org/10.1016/j.corsci.2021.109750>

### To cite this version:

Barroux, Adrien  and Delgado, Julien and Orazem, Mark E. and Tribollet, Bernard and Laffont, Lydia  and Blanc, Christine  *Electrochemical impedance spectroscopy study of the passive film for laser-beam-melted 17-4PH stainless steel*. (2021) Corrosion Science, 191. 109750. ISSN 0010-938X

Any correspondence concerning this service should be sent  
to the repository administrator: [tech-oatao@listes-diff.inp-toulouse.fr](mailto:tech-oatao@listes-diff.inp-toulouse.fr)

# Electrochemical impedance spectroscopy study of the passive film for laser-beam-melted 17-4PH stainless steel

A. Barroux<sup>a,b</sup>, J. Delgado<sup>c</sup>, M.E. Orazem<sup>d</sup>, B. Tribollet<sup>e</sup>, L. Laffont<sup>a</sup>, C. Blanc<sup>a,\*</sup>

<sup>a</sup> CIRIMAT, Université de Toulouse, CNRS, INP-ENSIACET, 4 allée Emile Monso, BP 44362, 31030, Toulouse cedex 4, France

<sup>b</sup> CETIM, Pôle Matériaux Métalliques et Surfaces, 74, route de la Jonelière CS 50814, 44308, Nantes, France

<sup>c</sup> CETIM, Pôle Matériaux Métalliques et Surfaces, 52 Avenue Félix Louat CS 80067, 60304, Senlis, France

<sup>d</sup> Department of Chemical Engineering, University of Florida, Gainesville, FL, 32611, USA

<sup>e</sup> LISE UMR 8235, CNRS-Sorbonne Universités, 4 Place Jussieu BP 133, 75252, Paris, France

## ARTICLE INFO

### Keywords:

- A. Stainless steel
- B. EIS
- B. Modelling studies
- C. Passive films
- C. Pitting corrosion

## ABSTRACT

The passive films formed on laser-beam-melted (LBM) and conventional 17-4PH martensitic stainless steels were studied by electrochemical impedance measurements in a 0.5 M NaCl solution at the corrosion potential. The passive films were described as dielectric layers, and impedance data showed that the Young model was the most appropriate to describe their electrical properties. Fitting of the impedance data led to lower capacitance values, associated with a thicker oxide layer, and higher resistivity values at the oxide-electrolyte interface for the LBM samples. While the differences were subtle, impedance measurements served to explain the better pitting corrosion resistance of LBM samples.

## 1. Introduction

In the last few years, additive manufacturing (AM) has emerged as a powerful means of producing metallic parts. Indeed, these new processes allow the fabrication of near-net-shaped structures of many metallic materials without prohibitive waste generation and with substantial time saving [1]. Additively manufactured (AM) steels have been largely studied, and abundant literature has been focused on the microstructures of AM steel components, and only a few very recent references have been given here [2–4]. However, very few papers concerned their corrosion properties, and the largest part of these concerned 316 L stainless steel (SS) [5–12]. The authors compared the corrosion properties of AM 316 SS to those of the wrought counterpart, and showed that substantial differences were observed between the two materials due to specific microstructures generated by AM processes. In most of the studies, authors showed that AM 316 SS showed a better corrosion behavior than its conventional counterpart due to its finer microstructure and absence of MnS inclusions [5–10]. In their review, Sander et al. [13] showed that only a few studies have been performed concerning the 17-4PH martensitic stainless steel (MSS), even though this ferrous alloy is widely used in a large variety of applications. These authors referred to the work of Schaller et al. [14] and Stoudt et al. [15]. They showed that the two studies led to contradictory results; this could

be explained by considering that Schaller's work was focused on the influence of porosities on the 17-4PH corrosion behavior, whereas, Stoudt et al. investigated the effect of post-build heat treatments. More globally, such a comment could be related to the complexity of the microstructures generated by AM processes. Indeed, studies focused on the microstructure of AM 17-4PH MSS showed that AM components contained microstructural defects, e.g., gas pores or lack-of-fusion pores, which were not observed in the wrought MSS [16,17]. Such microstructural defects could significantly influence the corrosion behavior, as shown by Schaller et al. [14], but also other authors for the 17-4PH MSS and other steels [18–20]. Furthermore, AM processes induced other changes in the microstructure of 17-4PH MSS, such as changes in the austenite to martensite ratio, martensite lath sizes, morphology and density of carbides [21,22], and all those parameters are likely to influence the corrosion behavior of the MSS. In our previous study [23], we compared the pitting corrosion behavior of a power-bed-laser-beam-melted (LBM) 17-4PH MSS to that of the conventional MSS. We showed that LBM 17-4PH MSS had more noble pitting potentials, which was related to smaller niobium carbides (NbCs) acting as preferential pitting sites, as compared to conventional MSS. In another study [24], we performed a combined X-ray photoelectron (XPS) spectroscopy and transmission electron microscopy (TEM) study of the passive films formed on both the LBM and conventional 17-4PH

\* Corresponding author.

E-mail address: [christine.blanc@ensiacet.fr](mailto:christine.blanc@ensiacet.fr) (C. Blanc).

MSSs. We showed that a similar two-layer structure of the passive film was observed for both MSSs, but the passive film formed on the conventional MSS was thinner and contained a higher Cr content as compared to the passive film formed on LBM MSS, due to the lower reversed austenite to martensite ratio in the conventional MSS as compared to the LBM MSS. Those results highlighted the interest of an in-depth analysis of the properties of the passive films formed on the conventional and LBM 17-4PH MSSs to contribute to explain their pitting corrosion behaviour.

Literature data exist concerning the structure and electrical properties of passive films formed on AM 316 SS [6–8,11,12], but, to our knowledge, nothing has been done concerning the AM 17-4PH MSS. A recent work of Revilla et al. [11] proposed an electrochemical impedance spectroscopy (EIS) study of the native oxide layer of AM 316 L SS by comparison to the wrought counterpart. The authors showed significant differences in dielectric properties and conductivity profiles of the oxide layers formed on the two steels. This study demonstrated once more the interest of EIS for the analysis of the electrical properties of the passive films, which has been previously shown for conventional metallic materials [25,26]. However, proper analysis of EIS data requires use of a process model, i.e., a model that could lead to a meaningful representation of the electrochemical system, with the hypothesis that these oxide layers are uniform and homogeneous in a plane parallel to the surface, but have a property gradient in a direction perpendicular to the surface. Veluchamy et al. provided a critical review of the models used to describe the mechanisms underlying passivity [27], showing that numerous models exist, but the mechanism are not well understood. Tribollet et al. [28] presented different models that can describe an oxide layer considered as a dielectric layer, in particular the Young and power-law models, both taking into account the variation in the resistivity of the passive film with respect to the normal distance to the sample surface. Those models have been extensively used in the literature to analyze EIS data for conventional materials [29–37]. Furthermore, the measurement model has also been shown to be useful to quantify the error structure of EIS measurements [38,39].

The objective of the present work is to take advantage of EIS to analyze the electrical properties of the passive film formed on a LBM 17-4PH MSS in comparison to its conventional counterpart. This will contribute to the development of a "database" within the literature concerning AM materials and their corrosion properties. EIS measurements were performed in NaCl solutions, and EIS data were analyzed by using, at the appropriate steps of the analysis, the measurement and Young models. The results are discussed in relation with our previous papers and literature data to contribute to an explanation of the corrosion properties of the LBM 17-4PH MSS in relation with its microstructure.

## 2. Experimental

LBM 17-4PH MSS cubic parts ( $20 \times 20 \times 20 \text{ mm}^3$ ) were fabricated from nitrogen-atomized powder provided by Erasteel. LBM part building was performed under argon atmosphere using an EOS M290 machine equipped with a 400 W laser, with the building plate maintained at 200 °C during the process. A 40- $\mu\text{m}$  layer thickness was maintained, and the laser power was between 351 W and 388 W leading to a hatching distance of 110  $\mu\text{m}$ . The laser strategy corresponded to a chessboard building with a 67-degree rotation between each layer. The building was in the z-direction, such that the XY plane was parallel to the building plate. For purpose of brevity, only this plane of the cube was studied in the present paper. For comparison purposes, samples removed from a 50-mm cylinder of a wrought 17-4 PH MSS provided by Bohler Edelstahl in H1025 metallurgical state were studied as a reference: they are referred to as conventional samples. LBM and conventional samples were removed from the core of the samples, i.e., cubes and cylinders, respectively, to avoid any influence of the edges, in particular any influence of the contouring strategy of the LBM process. The chemical

composition of LBM and conventional samples is given in Table 1. The samples were studied after H900 heat treatment, which corresponded to a solution heat treatment at 1040 °C for 30 min followed by air quenching, and then by an ageing at 480 °C for 1 h with final air quenching. The microstructures of both LBM and conventional MSSs were described in detail in a previous paper [23]. For brevity, only the main results are reported here after. For the LBM MSS, 50–800 nm wide martensite laths were observed, while, for the conventional MSS, the martensite laths were coarser with a width in the range [700 nm – 2.5  $\mu\text{m}$ ]. Furthermore, the LBM 17-4PH MSS contained finer NbCs precipitates as compared to the conventional MSS. Results also showed substantial differences in the austenite to martensite ratio between the two steels, with only 0.8 % of austenite for the conventional MSS, while the amount of austenite was  $\sim 12$  % in the XY plane of the LBM MSS. Finally, it was of interest to note that, on the basis of hydrostatic weighting analysis of the LBM samples, the porosity rate was calculated and was only 0.04 %, supporting the hypothesis that pores did not influence the corrosion behavior of the LBM samples, as shown by Barroux et al. [23].

EIS measurements were performed in a 0.5 M NaCl solution at 25 °C, stirred and open to air, by using a three-electrode cell, with a saturated calomel electrode (SCE) and a platinum foil, as reference and counter electrodes, respectively. The working electrode was LBM or conventional MSS sample, embedded in an epoxy resin, with a surface area exposed to the electrolyte of  $\sim 1 \text{ cm}^2$ . Before EIS measurements, the sample surface was mechanically ground with SiC paper down to 2400 grade and then polished with diamond paste down to 1  $\mu\text{m}$ . Finally, the surface was rinsed with deionized water in an ultrasonic bath. Two sets of EIS measurements were performed. The first one corresponded to the repetition of five EIS measurements performed consecutively with the same sample, i.e., the conventional sample, in order to calculate the error structure of the EIS measurements by using the measurement model. Before the first EIS measurement, the sample was maintained in the NaCl solution for 12 h at its open circuit potential (OCP) in order to reach near steady-state conditions. The second set of experiments consisted of EIS measurements performed after 12 h at OCP in 0.5 M NaCl solution for LBM and conventional samples. Samples were polished before each EIS measurement, and for each sample, the measurements were repeated three times to assess reproducibility. For all EIS measurements, the frequency range was from  $10^5 \text{ Hz}$  to  $10^{-2} \text{ Hz}$ , the potential modulation amplitude was 10 mV (rms), with 6 points per decade, and each average impedance value was calculated with 5 measurements per point.

The impedance data were regressed using a computer program published by Watson and Orazem [40]. The program allows measurement model analysis to identify the stochastic error structure of impedance measurements and to determine what part of the measurement is inconsistent with the Kramers-Kronig relations. The resulting data were subsequently regressed by an in-house simplex regression program.

## 3. Results

The impedance data were subjected to graphical analysis to provide an initial evaluation of the corresponding parameters. The measurement model was employed to assess the error structure of the data, and this information was used in regressing the process model, described in this section, to the experimental data. The organization of this part reflects the methodology applied.

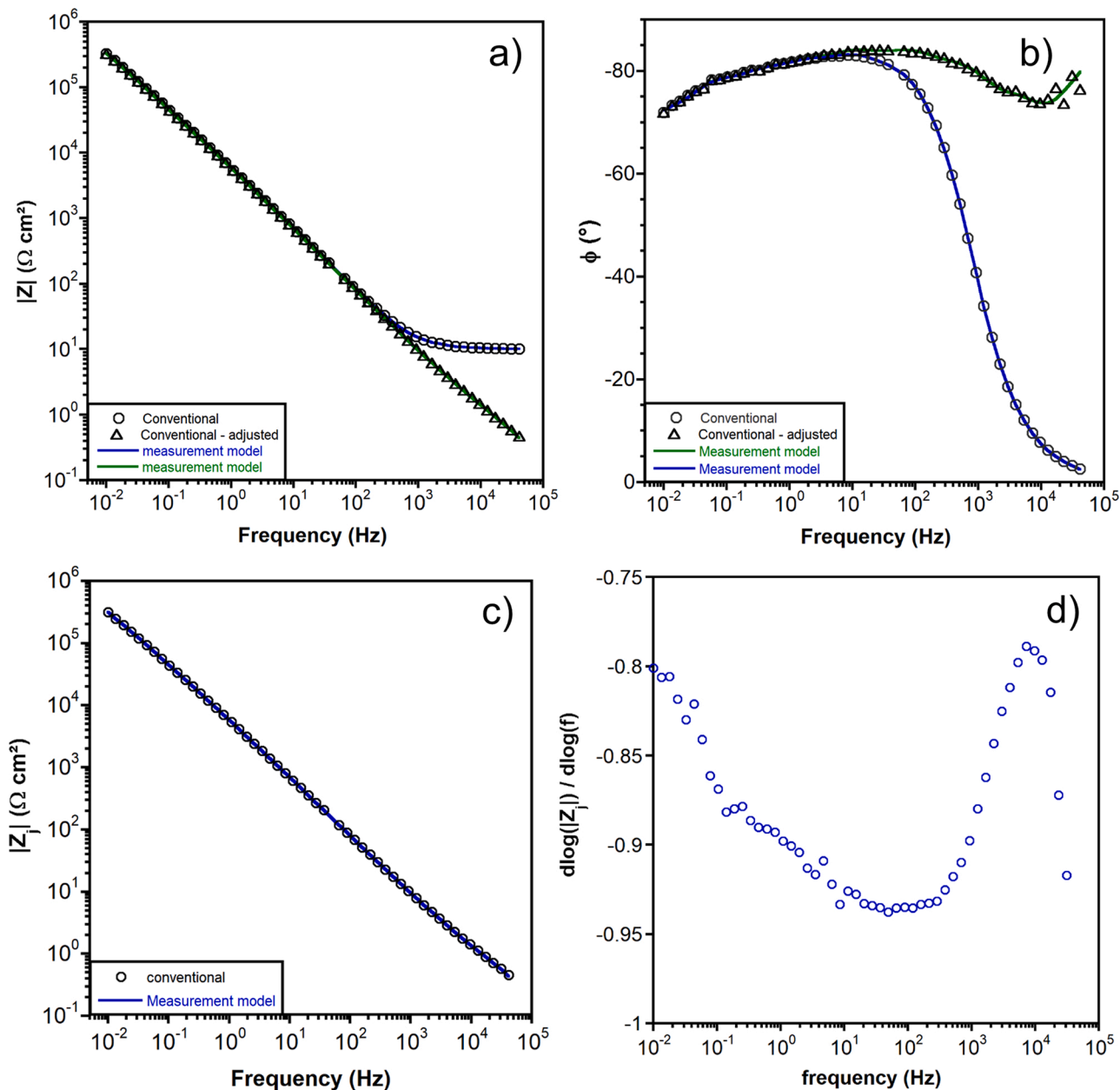
### 3.1. Qualitative analysis of EIS measurements

As an example, results from impedance measurements are plotted in Fig. 1 for the conventional steel. The results are presented on Bode plots and ohmic-resistance-corrected Bode plots (Fig. 1a and b). Corrected Bode plots correspond to the Bode plots of  $Z-R_e$  where  $R_e$ , the electrolyte

**Table 1**

Chemical composition of the LBM 17-4PH and conventional MSSs.

wt. %	Cr	Ni	Cu	C	Nb	Mn	Si	Mo	N	Fe
Conv.	15.42	4.49	3.24	0.036	0.26	0.39	0.35	0.15	0.030	bal.
LBM	16.20	4.08	3.56	0.028	0.27	0.32	0.71	≤ 0.02	0.035	bal.

**Fig. 1.** Bode plots and ohmic-resistance-corrected Bode plots in 0.5 M NaCl at  $E_{corr}$  for the conventional 17-4PH MSS: a) impedance modulus as a function of frequency, b) phase as a function of frequency, c)  $\log|Z_j|$  as a function of  $\log(f)$ , and d)  $d\log|Z_j|/d\log(f)$  as a function of  $\log(f)$ .

resistance, is estimated from the high-frequency data [30]. It is of interest to note that similar impedance diagrams were obtained for both MSSs. They both correspond to typical impedance data of a passive electrode under investigation. The data are also presented in the form  $\log|Z_j|$  as a function of  $\log(f)$  (Fig. 1c). The slope of the curve in Fig. 1c corresponds to the  $\alpha$  value of the CPE if the impedance could be analyzed with a CPE, given that, for a CPE, the  $\alpha$  value is independent of the frequency on a given frequency range [30]. From this curve, the figure  $d\log|Z_j|/d\log(f)$  as a function of  $\log(f)$  can be easily deduced (Fig. 1d). The results presented in Fig. 1d indicate the absence of

frequency-independent CPE behavior. Indeed, the phase of the corrected Bode plots (Fig. 1b) shows in high frequency a variation which corresponds to the ohmic impedance [31]. This ohmic impedance is the cause of the increase in the exponent value  $-d\log|Z_j|/d\log(f)$  for frequencies higher than 100 Hz.

### 3.2. Model used to describe the electrical properties of the passive films

Previous qualitative description of the impedance diagrams showed that EIS data were representative of the electrical properties of the

passive films formed on the MSSs. To go further in the investigation, EIS data were analyzed using the most appropriate model. In the present paper, we considered that the passive films formed on the LBM and conventional samples corresponded to dielectric layers, characterized by an impedance  $Z_0$  [28]. The layers were assumed to be homogeneous in a plane parallel to the sample surface. This constituted a simplifying hypothesis if we refer to our previous work [24]. Indeed, we showed, first, that the passive film formed on NbCs was different from this one formed on the martensitic matrix, which was true for both MSSs. Results also suggested differences in the passive films formed on austenitic grains from the one hand, and martensitic grains on the other hand. This was of major importance for the LBM samples which contained  $\sim 12\%$  of austenite. Therefore, this meant that the model should lead to mean properties in a plane parallel to the sample surface for both MSSs, in particular for LBM samples. Local impedance spectroscopy measurements should be necessary to take into account the heterogeneities in a plane parallel to the surface. However, as this was out of the scope of this study, we considered that a description of the mean properties in a plane parallel to the surface, but taking into account heterogeneities in the direction normal to the sample surface, constituted an interesting first approach for the LBM steel which has not been studied until now.

The equivalent circuit (Fig. 2a) also included the double-layer capacitance and a parallel resistance  $R_t$ . The parallel resistance corresponds to the electronic resistance  $R_{elec}$  of the passive film in series with the charge-transfer resistance  $R_{ct}$  associated with the cathodic oxygen reduction reaction at the electrolyte/passive film interface. The impedance diagrams also showed that the model needed to include the ohmic impedance  $Z_e$ , as defined in [31] and given by

$$Z_e = R_{HF} + \frac{R_{LF} R_{HF}}{(1 + (j\omega\tau)^\alpha)^{\alpha^*}} \quad (1)$$

where  $R_{HF}$  is the electrolyte resistance  $R_e$  at infinite frequency,  $R_{LF}$  is the low-frequency limit of the resistive behavior,  $\tau$  and  $\alpha^*$  are the two parameters corresponding to the distribution of time constant, and  $\alpha$  is added to take into account the frequency dispersion. Eq. 1 was verified for a disk electrode. In the present case, the electrode was rectangular, but, even if Eq. 1 could be different, the behavior is qualitatively the same. Therefore, the impedance of the electrochemical system  $Z$  was given by

$$Z = Z_e + \frac{1}{\frac{1}{Z_0} + \frac{1}{R_t}} \quad (2)$$

Finally, to account for the heterogeneity of the passive films in the

direction normal to the sample surface, a gradient in resistivity was assumed to exist from the underlying alloy/passive film interface to the passive film/electrolyte interface. In agreement with Tribollet et al. [28], such an oxide layer could be represented, with relevant physical meaning, by stacking several layers of similar thickness equal to  $d$ , each being characterized by a resistance  $R$  in parallel with a capacitance, such that the global passive film could be described by several RC circuits in series, the number of RC circuits depending on the resistivity profile of the passive film (Fig. 2b). In the literature, two resistivity profiles were proposed: a power-law model [25] and an exponential model [28]. The impedance corresponding to the power-law model presents a CPE behavior on a given frequency range, while the impedance corresponding to the Young impedance is not a CPE, but is characterized by a value of  $-\log|Z_j|/\log(f)$  that increases with frequency. The experimental data given in Fig. 1d corresponds to the Young model. Under the assumption that  $Z_0$  was well-represented by using the Young model [28], it could be given by

$$Z_0 = \frac{\lambda}{j\epsilon\epsilon_0} \ln \left[ \frac{1 + j\epsilon\epsilon_0\rho_0 \exp\left(\frac{\delta}{\lambda}\right)}{1 + j\epsilon\epsilon_0\rho_0} \right] \quad (3)$$

where  $\rho_0$  is the passive film resistivity at the underlying alloy/passive film interface,  $\delta$  the passive film thickness,  $\lambda$  is a characteristic distance of the resistivity profile,  $\epsilon$  is the dielectric constant, and  $\epsilon_0$  is the permittivity of vacuum. To fit the impedance data, it was easier to use  $\rho_\delta$  which corresponded to the passive film resistivity at the electrolyte/passive film interface, with  $\rho_\delta$  given by

$$\rho_\delta = \rho_0 \exp\left(\frac{\delta}{\lambda}\right) \quad (4)$$

The resistivity profile was then given by

$$\rho(x) = \rho_0 \exp\left(-\frac{x}{\lambda}\right) = \rho_\delta \exp\left(\frac{\delta - x}{\lambda}\right) \quad (5)$$

Eq. 5 shows that, with the Young model, the resistivity profile is a straight line in logarithmic scale.

### 3.3. Quantification of the error on the EIS measurements by using the measurement model

Before processing the Young model to the experimental data, the error structure of the data was determined by using the measurement model [40]. This model was developed to find first a way to account for

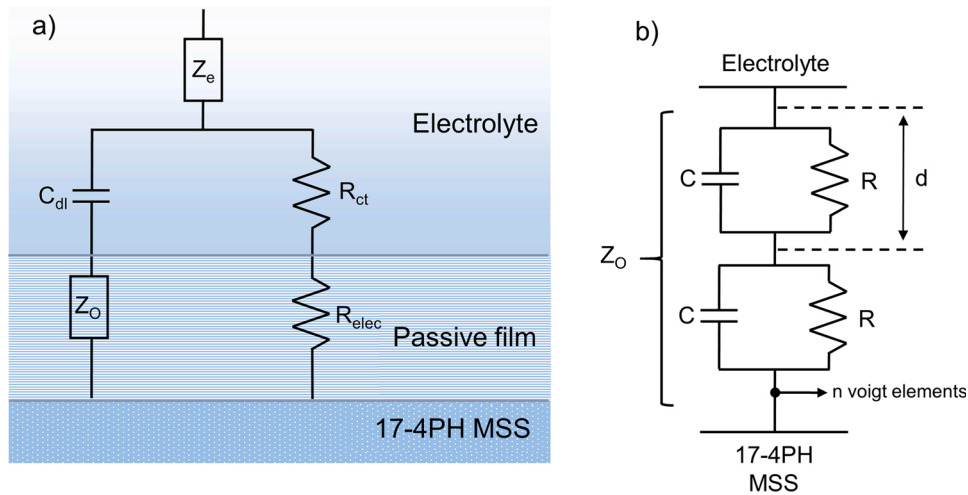


**Fig. 2.** Equivalent circuit used to model the electrochemical system: a) global circuit including the ohmic impedance given by Eq. 1 and the passive film impedance given by Eq. 3 and b) schematic description of the passive film layer as RC circuits in series to represent the heterogeneity of the layer in the direction normal to the sample surface.



measurement errors in the analysis of electrochemical impedance data while using relatively few parameters [41–43]. It is a circuit model consisting of a solution resistance in series with a number of Voigt elements – these Voigt elements are comprised of a resistor in parallel with a capacitor. The general structure for the measurement model to be regressed is

$$Z = R_e + Z_0 + R_e + \sum_{k=1}^n \frac{R_k}{1 + j\omega\tau_k} \quad (6)$$

where  $R_e$  is the electrolyte resistance,  $R_k$  is the  $k^{\text{th}}$  Voigt element resistance, and  $\tau_k$  is the  $k^{\text{th}}$  Voigt element time constant (equivalent to  $R_k C_k$ ). The corresponding equivalent circuit can be seen in Fig. 2b.

The principle behind using the measurement model to estimate the stochastic contribution to the error structure was presented by Agarwal et al. [44]. The complete error structure model is of the form

$$\sigma = \alpha_e |Z_j| + \beta_e |Z_r| + \gamma_e |Z|^2 + \delta_e \quad (7)$$

In the absence of internal sources of noise such as bubble generation, the stochastic noise is largely determined by the instrumentation. Thus, a single set of parameters  $\alpha_e$ ,  $\beta_e$ ,  $\gamma_e$ , and  $\delta_e$  should be sufficient to describe all impedance measurements conducted in a similar manner on a given instrument. To determine the error structure model, we used five replicate measurements: this was done for the conventional 17-4PH sample. In Fig. 3, the triangles and open circles represent the real part and the imaginary part, respectively, of the standard deviation in which the lack of reproducibility was filtered by the measurement-model technique. The line given in Fig. 3 is the fitted model for the error structure, i.e.,

$$\sigma = 0.003953 |Z_j| + 7.167 \cdot 10^{-9} |Z|^2 + 0.001499 \quad (8)$$

where  $\beta_e$  used in Eq. 7 was set equal to zero.

The error structure calculated for the conventional sample was assumed to be relevant for the LBM sample, considering that the impedance measurements were performed exactly in the same condi-

tions for both samples over identical frequency ranges. The regression of the Voigt measurement model yields capacitance, ohmic resistance, and polarization resistance values from impedance data. The capacitance of each Voigt element can be expressed as

$$C_k = \frac{\tau_k}{R_k} \quad (9)$$

When the frequency tends towards infinity, Eq. 6 becomes

$$Z = R_e + j \sum_{k=1}^n \frac{1}{\omega C_k} = R_e + \frac{j}{\omega C_{\text{eff}}} \quad (10)$$

where the effective capacitance can be obtained as

$$\frac{1}{C_{\text{eff}}} = \sum_{k=1}^n \frac{1}{C_k} \quad (11)$$

When the frequency tends towards zero, Eq. 6 becomes

$$Z = R_p + R_e + \sum_{k=1}^n R_k \quad (12)$$

where  $R_p = \sum_{k=1}^n R_k$  provides a value for the polarization resistance.

In the present study, only the parameters  $C_{\text{eff}}$  and  $R_e$  are needed to characterize the oxide layer. Their values are given in Table 2 for the three conventional samples and for the three LBM-XY samples. The corresponding fit with the measurement model is given in Fig. 4 and is quite good. It appears in Table 2 that the capacity values are a little bit larger for the conventional samples than for the LBM-XY samples. This could be interpreted as thinner passive films on conventional samples, by comparison to LBM samples, which should be in agreement with the lower modulus of the impedance for the conventional sample as compared to the LBM-XY sample (Fig. 4).

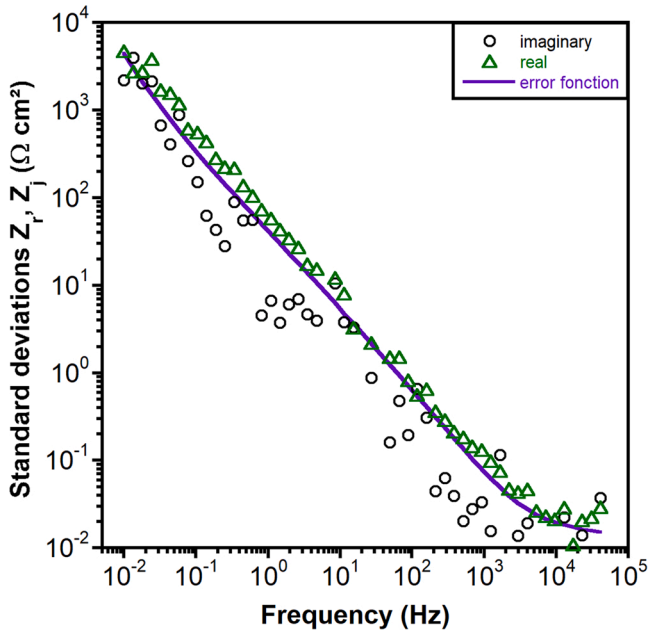
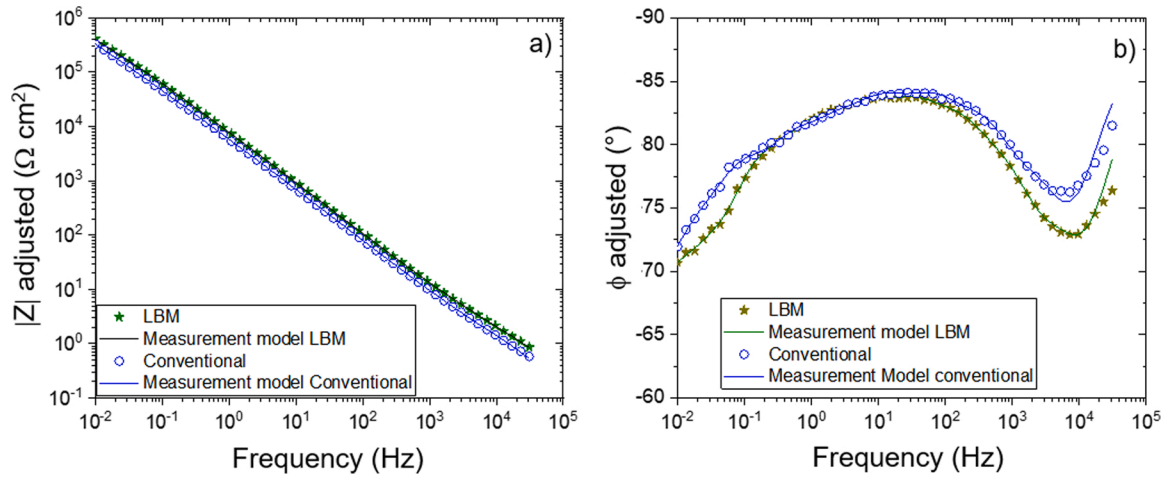


Fig. 3. Real and imaginary standard deviation of the stochastic part of impedance measurements obtained by application of the measurement model to impedance data obtained for the conventional sample in 0.5 M NaCl solution. The blue line is the fitted model for the error structure (Eq. 8) (For interpretation of the references to colour in this figure legend, the reader is referred to the web version of this article).

Table 2

Parameter values obtained by regression of the measurement and Young models to the impedance data ( $R_e$  values taken from the measurement model and  $\varepsilon = 12$  are used as input data for the Young model).

		Conv. -1	Conv. -2	Conv. -3
Measur. model	$C_{\text{MM}} (\mu\text{F cm}^{-2})$	$9.0 \pm 0.5$	$7.2 \pm 0.8$	$9.5 \pm 0.7$
	$R_e (\Omega \text{ cm}^2)$	$10.15 \pm 0.04$	$10.03 \pm 0.03$	$10.03 \pm 0.02$
	Number of fitted Voigt elements	7	10	10
	$C_{\text{YM}} (\mu\text{F cm}^{-2})$	8.36	9.65	10.21
Young model	$R_e (\Omega \text{ cm}^2)$	10.15	10.03	10.03
	$\rho_0 (\Omega \text{ cm}^{-1})$	2.66	1.58	2.5
	$\lambda (\text{nm})$	0.043	0.036	0.034
	$\delta (\text{nm})$	1.27	1.10	1.04
	$C_{\text{dl}} (\mu\text{F cm}^{-2})$	47.9	32.8	53.5
	$R_t (\text{M}\Omega \text{ cm}^2)$	2.13	1.11	2.12
		LBM XY -1	LBM XY -2	LBM XY -3
Measur. model	$C_{\text{MM}} (\mu\text{F cm}^{-2})$	$7.0 \pm 0.3$	$5.6 \pm 0.4$	$6.0 \pm 0.6$
	$R_e (\Omega \text{ cm}^2)$	$10.83 \pm 0.02$	$9.72 \pm 0.02$	$12.15 \pm 0.04$
	Number of fitted Voigt elements	9	11	9
	$C_{\text{YM}} (\mu\text{F cm}^{-2})$	8.23	9.15	7.13
Young model	$R_e (\Omega \text{ cm}^2)$	10.83	9.72	12.15
	$\rho_0 (\Omega \text{ cm}^{-1})$	111	59	15.4
	$\lambda (\text{nm})$	0.049	0.044	0.053
	$\delta (\text{nm})$	1.29	1.16	1.49
	$C_{\text{dl}} (\mu\text{F cm}^{-2})$	42.5	33.5	27.8
	$R_t (\text{M}\Omega \text{ cm}^2)$	2.53	0.92	1.69



**Fig. 4.** Ohmic-resistance-corrected Bode plots in 0.5 M NaCl at  $E_{\text{corr}}$  for the conventional 17-4PH and LBM MSSs: a) impedance modulus as a function of frequency and b) phase as a function of frequency. Impedance data were fitted with the measurement model by using the error structure calculated from impedance data of the conventional sample (Eq. 8).

### 3.4. Description of the resistivity profile of the passive film by using Young model

Due to the fact that a CPE was not evident in the entire frequency range (Fig. 1d), the Young model was used to analyze the experimental impedance data. In order to avoid the influence of the ohmic impedance, the experimental curves were regressed in the frequency range 0.01 Hz – 100 Hz. In this frequency range, the ohmic impedance is assumed to correspond to  $R_{\text{LF}}$ . For each sample,  $R_e$  values were those calculated by using the measurement model because they were the most accurate values that can be reached given that, for the Young model, the regression of the impedance data were done only for the low frequencies. Estimates for  $\rho_0$ ,  $\lambda$ , and  $\delta$  (Eq. 3) and  $C_{\text{dl}}$  and  $R_t = R_{\text{elec}} + R_{\text{ct}}$  (Fig. 2a) were obtained by an in-house simplex regression. As an example, the fitted curve and the experimental one are plotted in Fig. 5 for a conventional sample. Here also, both fitted and experimental curves are well-superimposed, and, for all samples, the results are similar. Regressed values are presented in Table 2. By using the usual formula, i.e.,

$$C_{\text{YM}} = \frac{\epsilon \epsilon_0}{\delta} \quad (13)$$

where  $\epsilon$  was assumed to be equal to 12, and  $\epsilon_0$  is the permittivity of

vacuum ( $8.85 \cdot 10^{-14}$  F/cm), the capacitance was determined, and values are given in Table 2. It can be noted that the capacitance values are a little bit larger than the values obtained with the measurement model. However, with both models, the values for the conventional samples are higher as compared to the LBM-XY samples, and as a consequence the corresponding thicknesses of the passive films are smaller for the conventional samples than for the LBM-XY samples.

The resistivity profiles obtained from the fitted parameters given in Table 2 (Eq. 5) are presented in Fig. 6. The resistivity profiles correspond to straight lines in semi-logarithmic coordinates, and the resistivity varies from an insulator at the metal-oxide interface to a semiconductor at the oxide-electrolyte interface. It could be reminded here that the oxygen reduction occurs at the oxide – electrolyte interface, where the oxide behaves as a semiconductor; then, the electron-transfer between this interface and the metal proceeds via the electronic resistance ( $R_{\text{elec}}$ ) of the oxide layer. The resistances associated to  $Z_0$ , calculated with the Young model, are ionic resistances linked to vacancies. Therefore, the resistivity profiles are associated with ionic resistivity. Results first showed a quite good repeatability of the resistivity profiles for both the conventional and LBM samples. Then, results also showed that the slopes of the resistivity profiles for LBM samples were slightly lower than those obtained for the conventional samples, such that the resistivity values for the LBM samples at the oxide-electrolyte interface were

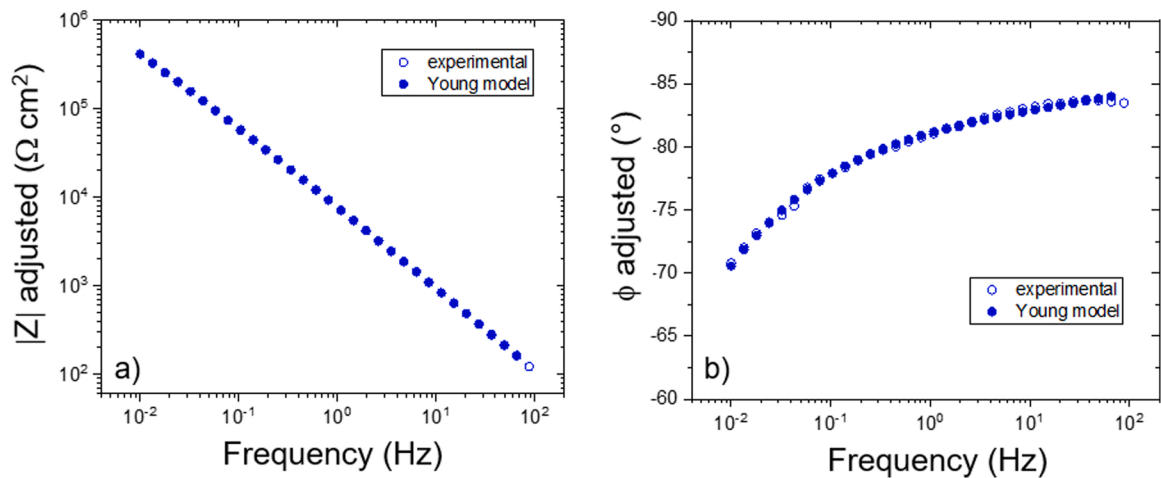


**Fig. 5.** Ohmic-resistance-corrected Bode plots in 0.5 M NaCl at  $E_{\text{corr}}$  for the conventional 17-4PH MSS for a reduced frequency range: a) impedance modulus as a function of frequency and b) phase as a function of frequency. Impedance data were fitted with the Young model. (color online only).



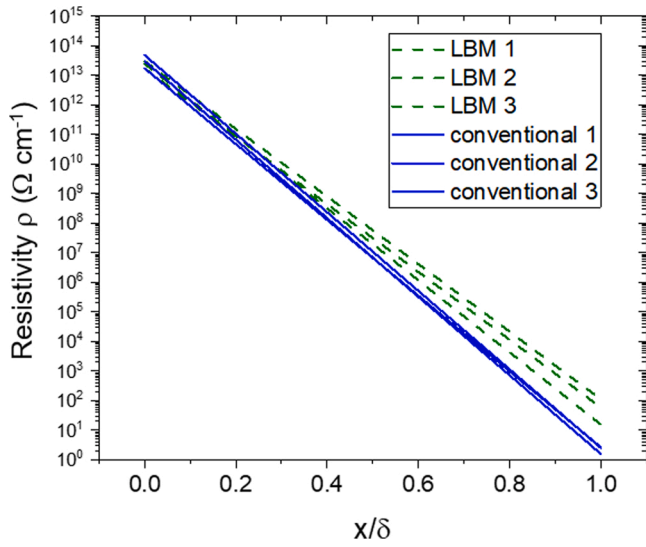


Fig. 6. Resistivity profiles obtained from the fitted parameters given in Table 2 for both the conventional and LBM 17-4PH MSSs.

slightly higher than for the conventional samples.

#### 4. Discussion

The objective of the present paper was to compare the electrical properties of the passive films formed on both LBM and conventional 17-4PH MSS samples. Results showed that the Young model was the most appropriate model to fit the impedance data obtained to characterize the electrical properties of the passive films formed on both LBM and conventional 17-4PH MSS samples. The Young model is associated with an exponential distribution of the resistivity through the passive films for both samples and is in agreement with results obtained by Revilla et al. for both AM and conventional 316 L SS [11]. Those authors obtained conductivity in the same order of magnitude than in the present study, and they showed that the conductivity profiles for the two samples were markedly different. In the present study, differences in the resistivity profiles obtained for the LBM and conventional 17-4PH MSSs were also observed, with resistivity values at the oxide-electrolyte interface higher for the LBM samples than for the conventional samples. Furthermore, in the present study, slightly higher capacitance values were obtained for the conventional 17-4PH MSS by comparison to LBM samples, in agreement with Revilla et al. [11].

Those higher capacitance values for the conventional samples led to thickness values  $\delta$  that were lower as compared to LBM samples. This result was in agreement with our previous results obtained by using both XPS and TEM [24]. Slight differences were noticeable, however, between the three sets of  $\delta$  values: 3.9 and 4.4 nm from XPS calculations,  $2.4 \pm 0.1$  nm and  $3.0 \pm 0.1$  nm from TEM measurements [24] and  $\sim 1.1$  nm and  $\sim 1.3$  nm from EIS data fitting for conventional and LBM MSSs, respectively (Table 2). The values given here from EIS data fitting are mean values calculated from the three  $\delta$  values given in Table 2 for both LBM and conventional samples. Concerning the differences between XPS and TEM thickness values, they were probably due to the different surface regions probed by the two techniques, and/or limitations of the equation used for XPS calculations. For EIS data fitting, it was of importance to note that  $\delta$  values were directly linked to the  $\epsilon$  values used. Here, the thickness was obtained by considering a value of 12 for the dielectric constant, which is a common value used in the literature. It was worth noting that, if the dielectric constant had a value of 25, as was reported by Revilla et al. [11], about the same thickness would be obtained by EIS and TEM. Nevertheless, we showed in previous study [24] that the differences in microstructure between the LBM and conventional samples led to the formation of a two-layer structure for the

passive films formed on both the conventional and LBM steels with, as previously reminded, differences in thickness, but also in chemical composition. Differences in compositional gradient in the passive film were shown, in particular concerning Cr distribution in both the inner and outer oxide layers [24]. These differences in compositional gradient should explain the differences in resistivity profiles shown in Fig. 6. This could in turn affect the dielectric properties of the passive film formed on the LBM samples and led to a different value of the dielectric constant by comparison to the conventional MSS. Therefore, the assumption that the dielectric constant for both LBM and conventional samples are equal may not provide the best approximation. For this reason, calculations were also done by using the values of passive film thickness ( $\delta$ ) obtained by using TEM as input data, i.e. 2.4 nm and 3.0 nm for conventional and LBM MSSs, respectively. In this case, the EIS experimental curves were regressed in the same frequency range 0.01 Hz – 100 Hz as before.  $R_e$  values were those calculated by using the measurement model. However, the three parameters fitted here were  $\rho_b$ ,  $\lambda$  and  $\epsilon$  (Eq. 3). Values are given in Table 3. Results showed that the dielectric properties were different for the passive films formed on the two MSSs, with mean  $\epsilon$  values of 26.3, close to the  $\epsilon$  value of 25 chosen by Revilla et al. [11], and 32.3 for the LBM and conventional MSSs, respectively. Those values were associated with higher capacitance values for the conventional samples as compared to the LBM samples, in agreement with both values from the measurement model and values from the Young model calculated using the first hypothesis (where  $\epsilon$  was fixed to 12).

The results obtained in the present study thus showed different electrical and dielectric properties of the passive films formed on LBM and conventional samples, associated with differences in thickness and composition. Concerning the thickness of the passive films, for all techniques, the  $\delta$  values corresponded to mean thickness values of the passive films formed on the MSS surfaces. The lower mean thickness of the passive films measured for the conventional samples could result from two contributions. Firstly, we showed in our previous study [24], by performing TEM observations at the scale of microstructural features, that the passive film formed on the NbCs was thinner, i.e. about 1.3 nm

Table 3

Parameter values obtained by regression of the measurement and Young models to the impedance data ( $R_e$  from the measurement model and  $\delta$  values of 2.4 nm and 3.0 nm for conventional and LBM MSSs, respectively, are used as input data for the Young model).

		Conv. -1	Conv. -2	Conv. -3
Measur. model	$C_{MM}$ ( $\mu F cm^{-2}$ )	$9.0 \pm 0.5$	$7.2 \pm 0.8$	$9.5 \pm 0.7$
	$R_e$ ( $\Omega cm^2$ )	$10.15 \pm 0.04$	$10.03 \pm 0.03$	$10.03 \pm 0.02$
	Number of fitted Voigt elements	7	10	10
	$C_{YM}$ ( $\mu F cm^{-2}$ )	10.32	12.54	12.90
Young model	$R_e$ ( $\Omega cm^2$ )	10.15	10.03	10.03
	$\rho_b$ ( $\Omega cm^{-1}$ )	305	161	430
	$\lambda$ (nm)	0.10	0.10	0.10
	$\epsilon$	28	34	35
	$C_{dl}$ ( $\mu F cm^{-2}$ )	47.9	30.3	53.5
	$R_t$ ( $M\Omega cm^2$ )	2.13	0.89	2.12
		LBM XY -1	LBM XY -2	LBM XY -3
Measur. model	$C_{MM}$ ( $\mu F cm^{-2}$ )	$7.0 \pm 0.3$	$5.6 \pm 0.4$	$6.0 \pm 0.6$
	$R_e$ ( $\Omega cm^2$ )	$10.83 \pm 0.02$	$9.72 \pm 0.02$	$12.15 \pm 0.04$
	Number of fitted Voigt elements	9	11	9
	$C_{YM}$ ( $\mu F cm^{-2}$ )	7.96	8.55	6.78
Young model	$R_e$ ( $\Omega cm^2$ )	10.83	9.72	12.15
	$\rho_b$ ( $\Omega cm^{-1}$ )	1.0	24.6	1.48
	$\lambda$ (nm)	0.10	0.12	0.10
	$\epsilon$	27	29	23
	$C_{dl}$ ( $\mu F cm^{-2}$ )	38.6	37.9	27.6
	$R_t$ ( $M\Omega cm^2$ )	2.54	1.43	1.69

thick, than that this one formed on the matrix. Therefore, the higher amount and larger size of NbCs in the conventional samples explained, at least partially, that the mean passive film thickness measured for the conventional samples was lower than for the LBM samples. Furthermore, the presence of a larger amount of reversed austenite in LBM 17-4PH MSS by comparison to the conventional sample should contribute to explain such a difference in the passive film thickness. Indeed, we showed in our previous study [24] that, because of lower Cr amount by comparison to martensitic grains, austenite grains are covered by a passive film containing less Cr leading to a global lower Cr amount in the passive film formed on 17-4PH LBM sample by comparison to conventional sample. This should be associated with differences in growth kinetics and resulting thickness of the passive films.

Clearly, it should be interesting to combine local TEM measurements of the passive film thickness (on NbCs, martensite and austenite grains), which should be highly time-consuming, with local EIS measurements, even though the relationship between the local EIS values and the nature of the microstructural features should not be trivial; but, this was not the scope of this study. The main results here were the good correspondence between XPS, TEM and EIS data, and therefore the determination of consolidated values of the mean thickness for the passive films formed on both conventional and LBM 17-4PH MSSs. The results were helpful in understanding the pitting behaviour of the 17-4PH MSSs. Indeed, the lower value for the mean thickness of the passive films on the conventional samples could be related to the less noble pitting potentials measured for those samples [23], even though, as expected, global EIS measurements do not give any direct data concerning local heterogeneities in the passive film, i.e. at NbCs, acting as preferential pit initiation sites [24], but provide only mean properties of this oxide film in a plane parallel to the sample surface.

Furthermore, the higher resistivity values at the oxide-electrolyte interface for the LBM samples could also contribute to justify the better resistance to pitting corrosion of those samples as compared to conventional samples. Finally, Macdonald et al. predicted, by using their point defect model, that solute/vacancy complexing was dependent on the dielectric constant of the passive film, with strongest complexing associated with lowest  $\epsilon$  values [45]. This also meant that the passive films characterized by the lowest  $\epsilon$  values were the most resistant to pitting corrosion, in agreement with the nobler pitting potential measured for LBM samples [23].

## 5. Conclusions

The main results obtained in the present study are the following:

- The passive films formed on both conventional and LBM 17-4PH MSSs could be described as dielectric layers, with an exponential variation of resistivity which was well-described by the Young model.
- Whatever the hypothesis used to make the regression of impedance data, impedance measurements showed higher capacitance values for the passive films formed on the conventional samples, as compared to LBM samples. Such values were related to thinner passive films on the conventional 17-4PH MSS as compared to the LBM MSS, in good agreement with previous XPS and global TEM analyses. Therefore, the EIS analysis of the passive films strengthened the previous XPS and TEM analyses. This corresponded to a global approach of the passive film thickness, i.e. to the determination of the mean thickness of the passive films.
- The lower value of the mean passive film thickness for the conventional MSS was assumed to be due, at least partially, to the lower amount of austenite in the conventional MSS associated with a globally higher Cr content in the passive film. It was also explained by more numerous and larger NbCs, considering that additional TEM investigations performed at a local scale highlighted a thinner passive film on NbCs as compared to the matrix.

- Differences in the resistivity profiles plotted for LBM and conventional samples were observed. The passive film formed on the LBM samples was characterized by higher resistivity values at the oxide-electrolyte interface, which should also contribute to explain its better pitting corrosion resistance.
- The regression of the impedance data, by using the TEM values of passive film thickness, allowed calculation of the dielectric constant ( $\epsilon$ ) values characteristic of the passive films. The lower  $\epsilon$  value obtained for the LBM sample might suggest also a better pitting corrosion resistance.

Finally, results showed that impedance measurements contributed to explain the lower resistance to pitting corrosion of the conventional 17-4PH MSS as compared to the LBM MSS.

## Author statement

**A. Barroux:** Investigations, Formal analysis, Validation, Visualization, Methodology, Data curation, Writing-Review&Editing.

**J. Delgado:** Funding acquisition (financial support), Resources (Materials), Project administration, Supervision.

**M.E. Orazem:** Conceptualization, Formal analysis, Methodology, Software, Validation, Writing - original draft, Writing - review & editing.

**B. Tribollet:** Conceptualization, Formal analysis, Methodology, Software, Validation, Visualization, Writing - original draft, Writing - review & editing.

**L. Laffont:** Supervision, Data curation, Writing-Review&Editing.

**C. Blanc:** Funding acquisition, Methodology, Formal analysis, Project administration, Supervision, Validation, Conceptualization, Data curation, Writing-original draft. Writing- Review & Editing.

## Data availability

The raw/processed data required to reproduce these findings cannot be shared at this time as the data also forms part of an ongoing study.

## Declaration of Competing Interest

The authors report no declarations of interest.

## Acknowledgments

The authors thank the ANRT for their financial support (Adrien Barroux's PhD thesis). Mark Orazem received financial support from the University of Florida Foundation Preeminence and the Dr. and Mrs. Frederick C. Edie term professorships.

## References

- [1] P. Kocovic, *History of additive manufacturing. 3D Printing and Its Impact on the Production of Fully Functional Components: Emerging Research and Opportunities*, IGI Global, Hershey, PA, 2017, pp. 1–24.
- [2] J. Chen, H. Wei, X. Zhang, Y. Peng, J. Kong, K. Wang, Flow behavior and microstructure evolution during dynamic deformation of 316 L stainless steel fabricated by wire and arc additive manufacturing, *Mater. Design* 198 (2021), 109325, <https://doi.org/10.1016/j.matdes.2020.109325>.
- [3] D. Yang, Y. Huang, J. Fan, M. Jin, Y. Peng, K. Wang, Effect of N<sub>2</sub> content in shielding gas on formation quality and microstructure of high nitrogen austenitic stainless steel fabricated by wire and arc additive manufacturing, *J. Manuf. Proc.* 61 (2021) 261–269, <https://doi.org/10.1016/j.jmapro.2020.11.020>.
- [4] P. Kohnen, S. Ewald, J.H. Schleifenbaum, A. Belyakov, C. Haase, Controlling microstructure and mechanical properties of additively manufactured high-strength steels by tailored solidification, *Addit. Manuf.* 35 (2020), 101389, <https://doi.org/10.1016/j.addma.2020.101389>.
- [5] R.I. Revilla, M. Van Calster, M. Raes, G. Arroud, F. Andreatta, L. Pyl, P. Guillaume, I. De Graeve, Microstructure and corrosion behavior of 316L stainless steel prepared using different additive manufacturing methods: a comparative study bringing insights into the impact of microstructure on their passivity, *Corros. Sci.* 176 (2020), 108914, <https://doi.org/10.1016/j.corsci.2020.108914>.

- [6] F. Andreatta, A. Lanzutti, E. Vaglio, G. Totis, M. Sortino, L. Fedrizzi, Corrosion behaviour of 316L stainless steel manufactured by selective laser melting, *Mater. Corr.* 70 (2019) 1633–1645, <https://doi.org/10.1002/maco.201910792>.
- [7] M.J.K. Lodhi, K.M. Deen, M.C. Greenlee-Wacker, W. Haider, Additively manufactured 316L stainless steel with improved corrosion resistance and biological response for biomedical applications, *Addit. Manuf.* 27 (2019) 8–19, <https://doi.org/10.1016/j.addma.2019.02.005>.
- [8] M.J.K. Lodhi, K.M. Deen, W. Haider, Corrosion behavior of additively manufactured 316L stainless steel in acidic media, *Mater.* 2 (2018) 111–121, <https://doi.org/10.1016/j.mtl.2018.06.015>.
- [9] C. Man, C. Dong, T. Liu, D. Kong, D. Wang, X. Li, The enhancement of microstructure on the passive and pitting behaviors of selective laser melting 316L SS in simulated body fluid, *Appl. Surf. Sci.* 467–468 (2019) 193–205, <https://doi.org/10.1016/j.apsusc.2018.10.150>.
- [10] D. Kong, C. Dong, X. Ni, L. Zhang, H. Luo, R. Li, L. Wang, C. Man, X. Li, The passivity of selective laser melted 316L stainless steel, *Appl. Surf. Sci.* 504 (2020), 144495, <https://doi.org/10.1016/j.apsusc.2019.144495>.
- [11] R.I. Revilla, B. Wouters, F. Andreatta, A. Lanzutti, L. Fedrizzi, I. De Graeve, EIS comparative study and critical Equivalent Electrical Circuit (EEC) analysis of the native oxide layer of additive manufactured and wrought 316L stainless steel, *Corr. Sci.* 167 (2020), 108480, <https://doi.org/10.1016/j.corsci.2020.108480>.
- [12] N.S. Al-Mamun, W. Haider, I. Shabib, Corrosion resistance of additively manufactured 316L stainless steel in chloride – thiosulfate environment, *Electrochim. Acta* 362 (2020), 137039, <https://doi.org/10.1016/j.electacta.2020.137039>.
- [13] G. Sander, J. Tan, P. Balan, O. Gharbi, D.R. Feenstra, L. Singer, S. Thomas, R. G. Kelly, J.R. Scully, N. Birbilis, Corrosion of additively manufactured alloys: a review, *Corrosion* 74 (2018) 1318–1350, <https://doi.org/10.5006/2926>.
- [14] R.F. Schaller, J.M. Taylor, J. Rodelas, E.J. Schindelholz, Corrosion properties of powder bed fusion additively manufactured 17-4 PH stainless steel, *Corrosion* 73 (2017) 796–807, <https://doi.org/10.5006/2365>.
- [15] M.R. Stoudt, R.E. Ricker, E.A. Lass, L.E. Levine, The influence of post-build microstructure on the electrochemical behavior of additively manufactured 17-4 PH stainless steel, *JOM* 69 (2017) 506–515, <https://doi.org/10.1007/s11837-016-2237-y>.
- [16] P. Leo, S. D'Ostuni, P. Perulli, M.A.C. Sastre, A.I. Fernández-Abia, J. Barreiro, Analysis of microstructure and defects in 17-4 PH stainless steel sample manufactured by Selective Laser Melting, *Procedia Manuf.* 41 (2019) 66–73, <https://doi.org/10.1016/j.promfg.2019.07.030>.
- [17] H. Irrinki, J.S.D. Jangam, S. Pasebani, S. Badwe, J. Stitzel, K. Kate, O. Gulsoy, S. V. Atre, Effects of particle characteristics on the microstructure and mechanical properties of 17-4 PH stainless steel fabricated by laser-powder bed fusion, *Powder Technol.* 331 (2018) 192–203, <https://doi.org/10.1016/j.powtec.2018.03.025>.
- [18] M.A. Melia, H.-D.A. Nguyen, J.M. Rodelas, E.J. Schindelholz, Corrosion properties of 304L stainless steel made by directed energy deposition additive manufacturing, *Corros. Sci.* 152 (2019) 20–30, <https://doi.org/10.1016/j.corsci.2019.02.029>.
- [19] M. Laleh, A.E. Hughes, S. Yang, J. Li, W. Xu, I. Gibson, M.Y. Tan, Two and three-dimensional characterisation of localised corrosion affected by lack-of-fusion pores in 316L stainless steel produced by selective laser melting, *Corros. Sci.* 165 (2020), 108394, <https://doi.org/10.1016/j.corsci.2019.108394>.
- [20] H.R. Lashgari, Y. Xue, C. Onggowarsito, C. Kong, S. Li, Microstructure, tribological properties and corrosion behaviour of additively manufactured 17-4PH stainless steel: effects of scanning pattern, build orientation, and single vs. Double scan, *Mater. Today Com.* 25 (2020), 101535, <https://doi.org/10.1016/j.mtcomm.2020.101535>.
- [21] L.E. Murr, E. Martinez, J. Hernandez, S. Collins, K.N. Amato, S.M. Gaytan, P. W. Shindo, Microstructures and properties of 17-4 PH stainless steel fabricated by selective laser melting, *J. Mater. Res. Technol.* 1 (2012) 167–177, [https://doi.org/10.1016/S2238-7854\(12\)70029-7](https://doi.org/10.1016/S2238-7854(12)70029-7).
- [22] Y. Sun, R.J. Hebert, M. Aindow, Effect of heat treatments on microstructural evolution of additively manufactured and wrought 17-4PH stainless steel, *Mater. & Design* 156 (2018) 429–440, <https://doi.org/10.1016/j.matdes.2018.07.015>.
- [23] A. Barroux, N. Ducommun, E. Nivet, L. Laffont, C. Blanc, Pitting corrosion of 17-4PH stainless steel manufactured by laser beam melting, *Corros. Sci.* 169 (2020), 108594, <https://doi.org/10.1016/j.corsci.2020.108594>.
- [24] A. Barroux, T. Duguet, N. Ducommun, E. Nivet, J. Delgado, L. Laffont, C. Blanc, Combined XPS/TEM study of the chemical composition and structure of the passive film formed on additive manufactured 17-4PH stainless steel, *Surf. Interf.* 22 (2021), 100874, <https://doi.org/10.1016/j.surfin.2020.100874>.
- [25] M.E. Orazem, I. Frateur, B. Tribollet, V. Vivier, S. Marcelin, N. Pebere, A.L. Bunge, E.A. White, D.P. Riemer, M. Musiani, Dielectric properties of materials showing constant-phase-element (CPE) impedance response, *J. Electrochem. Soc.* 160 (2013) C215–C225, <https://doi.org/10.1149/2.033306jes>.
- [26] C.M. Abreu, M.J. Cristóbal, R. Losada, X.R. Nóvoa, G. Pena, M.C. Pérez, Comparative study of passive films of different stainless steels developed on alkaline medium, *Electrochim. Acta* 49 (2004) 3049–3056, <https://doi.org/10.1016/j.electacta.2004.01.064>.
- [27] A. Veluchamy, D. Sherwood, E. Bosco, I.S. Cole, Critical review on the passive film formation and breakdown on iron electrode and the models for the mechanisms underlying passivity, *J. Electroanal. Chem.* 785 (2017) 196–215, <https://doi.org/10.1016/j.jelechem.2016.12.020>.
- [28] B. Tribollet, V. Vivier, M.E. Orazem, EIS technique in passivity studies: determination of the dielectric properties of passive films, *Encyclopedia of Interfacial Chemistry: Surface Science and Electrochemistry*, Elsevier, 2017, pp. 1–14.
- [29] T.T.M. Tran, B. Tribollet, E.M.M. Sutter, New insights into the cathodic dissolution of aluminium using electrochemical methods, *Electrochim. Acta* 216 (2016) 58–67, <https://doi.org/10.1016/j.electacta.2016.09.011>.
- [30] M.E. Orazem, N. Pebère, B. Tribollet, Enhanced graphical representation of electrochemical impedance data, *J. Electrochem. Soc.* 153 (2006) B129–B136, <https://doi.org/10.1149/1.2168377>.
- [31] O. Gharbi, A. Dizon, M.E. Orazem, M.T.T. Tran, B. Tribollet, V. Vivier, From frequency dispersion to ohmic impedance: a new insight on the high-frequency impedance analysis of electrochemical systems, *Electrochim. Acta* 320 (2019), 134609, <https://doi.org/10.1016/j.electacta.2019.134609>.
- [32] S. Marcelin, B. Ter-Ovanesian, B. Normand, Electronic properties of passive films from the multi-frequency Mott–Schottky and power-law coupled approach, *Electrochem. Com.* 66 (2016) 62–65, <https://doi.org/10.1016/j.electcom.2016.03.003>.
- [33] M. Musiani, M.E. Orazem, N. Pebère, B. Tribollet, V. Vivier, Determination of resistivity profiles in anti-corrosion coatings from constant-phase-element parameters, *Prog. Org. Coat.* 77 (2014) 2076–2083, <https://doi.org/10.1016/j.porgcoat.2013.12.013>.
- [34] B. Hirschorn, M.E. Orazem, B. Tribollet, V. Vivier, I. Frateur, M. Musiani, Determination of effective capacitance and film thickness from constant-phase-element parameters, *Electrochim. Acta* 55 (2010) 6218–6227, <https://doi.org/10.1016/j.electacta.2009.10.065>.
- [35] B. Hirschorn, M.E. Orazem, B. Tribollet, V. Vivier, I. Frateur, M. Musiani, Constant-phase-Element behavior caused by resistivity distributions in films I. Theory, *J. Electrochem. Soc.* 157 (2010) C452–C457, <https://doi.org/10.1149/1.3499564>.
- [36] B. Hirschorn, M.E. Orazem, B. Tribollet, V. Vivier, I. Frateur, M. Musiani, Constant-phase-Element behavior caused by resistivity distributions in films II. Applications, *J. Electrochem. Soc.* 157 (2010) C458–C463, <https://doi.org/10.1149/1.3499565>.
- [37] M.E. Orazem, I. Frateur, B. Tribollet, V. Vivier, S. Marcelin, N. Pebère, A.L. Bunge, E.A. White, D.P. Riemer, M. Musiani, Dielectric properties of materials showing constant-phase-Element (CPE) impedance response, *J. Electrochem. Soc.* 160 (2013) C215–C225, <https://doi.org/10.1149/2.033306jes>.
- [38] H. Liao, W. Watson, A. Dizon, B. Tribollet, V. Vivier, M.E. Orazem, Physical properties obtained from measurement model analysis of impedance measurements, *Electrochim. Acta* 354 (2020), 136747, <https://doi.org/10.1016/j.electacta.2020.136747>.
- [39] P. Agarwal, O.D. Crisalle, M.E. Orazem, L.H. García-Rubio, Measurement Models for Electrochemical Impedance Spectroscopy: 2. Determination of the Stochastic Contribution to the Error Structure, *J. Electrochem. Soc.* 142 (1995) 4149–4158, <https://doi.org/10.1149/1.2048478>.
- [40] W. Watson, M.E. Orazem, EIS: Measurement Model Program, ECSArXiv, 2020. <https://ecsarxiv.org/kze9x/>.
- [41] P. Agarwal, M.E. Orazem, L.H. García-Rubio, Measurement Models for Electrochemical Impedance Spectroscopy: 1. Demonstration of Applicability, *J. Electrochem. Soc.* 139 (1992) 1917–1927, <https://doi.org/10.1149/1.2069522>.
- [42] P. Agarwal, O.D. Crisalle, M.E. Orazem, L.H. García-Rubio, Application of Measurement Models to Electrochemical Impedance Spectroscopy: 2. Determination of the Stochastic Contribution to the Error Structure, *J. Electrochem. Soc.* 142 (1995) 4149–4158, <https://doi.org/10.1149/1.2048478>.
- [43] P. Agarwal, M.E. Orazem, L.H. García-Rubio, Application of Measurement Models to Electrochemical Impedance Spectroscopy: 3. Evaluation of Consistency with the Kramers-Kronig Relations, *J. Electrochem. Soc.* 142 (1995) 4159–4168, <https://doi.org/10.1149/1.2048479>.
- [44] P. Agarwal, O.C. Moghissi, M.E. Orazem, L.H. García-Rubio, Application of measurement models for analysis of impedance spectra, *Corrosion* 49 (1993) 278–289, <https://doi.org/10.5006/1.3316050>.
- [45] M. Urquidí-Macdonald, D.D. Macdonald, Theoretical analysis of the effects of alloying elements on distribution functions of passivity breakdown, *J. Electrochem. Soc.* 136 (1989) 961–967.